A Simulation Study of Ionizing Radiation Acoustic Imaging (iRAI) as a Real-Time Dosimetric Technique for Ultra High Dose Rate Radiotherapy (UHDR-RT)

Noora H Ba Sunbul (corr-auth)[1,2], Wei Zhang[3], Ibrahim Oraiqat[2,5], Dale Litzenberg[2], Kwok Leung Lam[2], Kyle Cuneo[2], Jean M Moran -EBM[2], Paul L. Carson[3], Xueding Wang[3], Shaun D Clarke[1], Martha Marie Matuszak[1,2], Sara A Pozzi[1], Issam El Naqa -EBM[2,5]

[1] Department of Nuclear Engineering and Radiological Sciences, University of Michigan, Ann Arbor, Michigan

[2] Department of Radiation Oncology, University of Michigan, Ann Arbor, Michigan

[3] Department of Biomedical Engineering, University of Michigan, Ann Arbor, Michigan

[4] Department of Radiology, University of Michigan, Ann Arbor, Michigan

[5] Department of Machine Learning, Moffitt Cancer Center, Tampa, Florida

Running title: Radiation Acoustic Imaging for UHDR-RT

* Corresponding author: nooraba@umich.edu. ; 2355 Bonisteel Blvd, Ann Arbor, MI 48109.

ABSTRACT

Purpose: Electron-based ultra-high dose rate radiation therapy (UHDR-RT), also known as Flash-RT, has shown the ability to improve the therapeutic index in comparison to conventional radiotherapy (CONV-RT) through increased sparing of normal tissue. However, the extremely high-dose rates in UHDR-RT have raised the need for accurate real-time dosimetry tools. This work aims to demonstrate the potential of the emerging technology of Ionized Radiation Acoustic Imaging (iRAI) through simulation studies and investigate its characteristics as a promising relative *in vivo* dosimetric tool for UHDR-RT.

Methods: The detection of induced acoustic waves following a single UHDR pulse of a modified 6 MeV 21EX Varian Clinac in a uniform porcine gelatin phantom that is brain-tissue equivalent was simulated for an ideal ultrasound transducer. The full 3D dose distributions in the phantom for a 1x1 cm^2 field were simulated using EGSnrc (BEAMnrc\DOSXYZnrc) Monte Carlo (MC) codes. The relative dosimetry simulations were verified with dose experimental measurements using Gafchromic films. The spatial dose distribution was converted into an initial pressure source spatial distribution using the medium dependent dose-pressure relation. The MATLAB based toolbox k-Wave was then used to model the propagation of acoustic waves through the phantom and perform time-reversal (TR) based imaging reconstruction. The effect of the various linear accelerator (linac) operating parameters, including linac pulse duration and pulse repetition rate (frequency), were investigated as well.

Results: The Monte Carlo dose simulation results agreed with the film measurement results, specifically at the central beam region up to 80% dose within approximately 5% relative error for the central profile region and a local relative error of < 6 % for percentage dose depth. IRAI-based FWHM of the radiation beam was within approximately 3 mm relative to the MC simulated beam FWHM at the beam entrance. The real time pressure signal change agreed with the dose changes proving the capability of the iRAI for predicting the beam position. IRAI was tested through 3D simulations of its response to be based on the temporal changes in the linac operating parameters on a dose per pulse basis as expected theoretically from the pressure-dose proportionality. The pressure signal amplitude obtained through 2D simulations was proportional to the dose per pulse. The instantaneous pressure signal amplitude decreases as the linac pulse duration increases, as predicted from the pressure wave generation equations, such that the shorter the linac pulse the higher the signal and the better the temporal (spatial) resolutions of iRAI. The effect of the longer linac pulse duration on the spatial resolution of the 3D constructed iRAI images was corrected for through linac pulse deconvolution. This correction has improved the passing rate of the 1%/1mm gamma test criteria, between the pressure-constructed and dosimetric beam characteristic, to as high as 98%.

Conclusions: A full simulation workflow was developed for testing the effectiveness of iRAI as a promising relative dosimetry tool for UHDR-RT radiation therapy. IRAI has shown the advantage of 3D dose mapping through the dose signal linearity and hence has the potential to be a useful dosimeter at depth dose measurement and beam localization and hence potentially for *in vivo* dosimetry in UHDR-RT.

Index Terms— UHDR (Flash) radiotherapy, Monte Carlo, Radiation acoustics, *in vivo* dosimetry.

Introduction

Ultra-high dose rate irradiation UHDR-RT, also known as Flash, involves high treatment dose rates (average dose rates > 40 Gy/s) that are a few hundred times larger than those in conventional radiation therapy [1]. Based on preclinical studies, UHDR-RT has shown potential in increasing the therapeutic index by decreasing normal tissue toxicity (normal tissue sparing effect) while maintaining the same dose per pulse tumor killing effectiveness [2–6,7].

This preclinically proven advantage of ultra-high dose treatment has increased the potential for its applicability in radiation therapy. Additionally, the higher dose delivery results in overall shorter treatment times of 0.1 s or shorter [1]. A recent clinical study was performed on a cutaneous lymphoma treated with a single 15 Gy UHDR-RT fraction in only 90 milliseconds [8]. This instantaneous dose delivery advantage of UHDR-RT is expected to mitigate the intra-fraction patient motion effect, which will result in more precise and efficient treatment delivery. Additionally, UHDR-RT will be more efficient by treating more patients at shorter treatment delivery time with better therapeutic index.

One of the main challenges of preclinical research is the limited availability of research accelerators and machines that can operate in the UHDR mode. To mitigate this limitation, several groups have developed techniques to use commercially available research and clinical linacs in UHDR irradiations of small animals[1,9].

Because a high dose is delivered during each pulse of UHDR-RT, more accurate dosimetry tools are needed to support a per pulse basis compared to conventional RT. There is currently no available on-line dosimeter that can be used for electron dosimetry on a dose per pulse basis and detect dose rates in the UHDR range given their sensitive dose rate threshold. The high dose per pulse rates of UHDR-RT has resulted in dose saturation problems with commonly used dosimeters. For instance, ionization chambers have shown ion recombination problems at higher dose per pulse values. While semiconductors showed uncorrectable saturation for UHDR dose rates [10]. Active work is currently ongoing to identify suitable online dosimeters for UHDR dosimetry. For a clinical dosimeter to be implemented in UHDR-RT for in-depth treatment delivery monitoring, it is desirable to use advanced dosimetry techniques that are able to also provide real-time (*in vivo*) readouts per linac pulse beyond superficial depths for internal dose monitoring and beam localization.

Ionizing radiation acoustic imaging (iRAI) is an imaging modality that constructs dose-related images based on acoustic waves induced by ionizing radiation through the thermoacoustic effect. As a pulsed beam of ionizing radiation (e.g., electrons, photons, or protons) causes an excitation of the irradiated sample, this results in localized heating (< mK) [11]. This temperature increase results in thermoelastic expansion, which causes the generation of a differential pressure distribution. The generated differential pressure distribution is dependent on both the material properties of the medium exposed to the radiation beam as well as the radiation beam itself. With the presence of suitable detection

devices such as ultrasound transducers and hydrophones, the induced pressure gradients (mechanical stress/pressure) can be converted into electrical signals. The detected instantaneous (time-varying) pressure signals generate information regarding the initial pressure distribution that was induced following a pulse of radiation. A corresponding image of the initial pressure distribution, as a result, can be reconstructed using the induced acoustic signals acquired at multiple projections (angles) surrounding the irradiated region.

Since it was first proposed for tomographic imaging in 2013, the feasibility and clinical potential of iRAI has been investigated and demonstrated in many biomedical applications by different research groups worldwide[11–22]. The main areas of applicability of iRAI that have been investigated in the literature are relative and in vivo dosimetry for conventional photon therapy, localization of the Bragg peak in proton therapy, and as a low-dose medical imaging modality [13]. The feasibility of iRAI as an *in vivo* dosimeter during conventional external beam radiation therapy has been explored and demonstrated in several previous studies [12–14]. An animal study investigating the feasibility of iRAI was recently published showing that a proposed dual ultrasound-based image-guided radiotherapy system holds great potential for personalized cancer treatment and better outcomes [23].

The main characteristics of iRAI that make it a promising dosimetry technique are the dose and induced pressure linearity in addition to energy and dose rate independency. Although iRAI is independent of the average dose rate of the linac (i.e in Gy/min or Gy/s), the acoustic signal for each radiation pulse is dependent on the instantaneous dose rate during the pulse (i.e, Gy/pulse/s). The acoustic signal is hence proportional to the dose deposited in that radiation pulse. Additionally, the iRAI transducer is placed outside of the radiation beam field and therefore does not perturb the radiation beam, eliminating the need for perturbation correction factors [13].

With proper acoustical system, aperture and bandwidth configuration, iRAI as a thermoacoustic imaging modality can directly measure locally absorbed thermal energy, i.e., deposited dose in per pulse basis. Thus, this technique can offer intriguing promise for

implementation in UHDR dose per pulse detection without signal degradation. In this work, the feasibility of iRAI as a novel dosimetry tool for UHDR-RT is tested through computer simulations. K-wave simulation was used to model the electron-induced acoustic signal generation, propagation, and attenuation in a homogeneous porcine gelatin phantom. Then, the time-reversal algorithm was used to construct 3D iRAI images in different setups. This simulation study aims to verify the feasibility of the iRAI modality for relative UHDR-RT dosimetry and provide theoretical support for the experimentally measured results.

Methods and Material

A. Theory

Dose deposition and temperature increase

As a beam of ionizing radiation hits the medium, the radiation dose is deposited and is converted into heat energy. A pulsed electron beam is used as the ionizing radiation source in this article. The incident electron beam interacts with either the orbital electrons of the exposed medium or with the nuclei of the medium. This interaction results in atom ionization and/or excitation together with electron scattering either elastic or inelastic. The electron deacceleration results in generating X-ray photons (bremsstrahlung). The electron energy losses, which determine the electron range, are characterized by mass stopping power (S/ρ). During each pulse of the incident electron beam, the electronic stopping power is the main contributor to the local deposited dose per pulse [15,24]:

$$D_r(r,t) = \phi(r,t)(\frac{S}{\rho})_{el}, \qquad (1)$$

where, $D_r(r,t)$ is the dose rate deposition during an electron pulse (Gy/pulse/s), $\emptyset(r,t)$ is the electron fluence rate, the number of electrons produced during a pulse per unit area per unit time; S is the loss of the kinetic energy of the electron per unit length; and ρ is the density of the medium. The "el"

subscript refers to the electronic (ionization) mass stopping power. The local heat deposited due to the radiation dose is given by [15,24]:

$$H(r,t) = \eta_{th} \rho D_r(r,t) \tag{2}$$

Where $H(r,t)$ is the heat absorption rate per unit volume at position $r \in R^3$ and time t and η_{th} refers to the thermal heat efficiency. Heat efficiency refers to the amount of deposited radiation energy transferred to heat energy, and hence contributes to a temperature increase and it depends on the type of ionizing radiation and material being irradiated. Chemical reactions is the primary contributor to the reduction in heat efficiency. A small amount of the deposited radiation energy also goes into radiation-induced acoustic and optical emissions which contribute to additional reduction in heat efficiency [25].

Initial pressure generation and propagation:

The wave equation governs the generation of the electron-induced acoustic pressure, as well as its propagation in the medium, and is given by the thermoacoustic equation [15,24]:

$$(\nabla^2 - \frac{1}{v_s^2}\frac{\partial^2}{\partial t^2})p(r,t) = -\frac{\beta K_T \eta_{th}}{v_s^2 C_v}\frac{\partial D_r(r,t)}{\partial t}, \tag{3}$$

where β is the volumetric thermal expansion coefficient, K_T is the isothermal bulk modulus and $v_s = \sqrt{K_T/\rho}$ (in m/s) is the speed of sound in the medium. The dose (or fluence) rate of a single electron pulse can be treated as a Dirac delta function by selecting a low-frequency acoustic detection range, which leads to lower spatial resolution, to satisfy the stress confinement condition ($\tau_e \cdot v_s \ll$ spatial resolution), where τ_e is the linac pulse duration. Since clinical linacs have a relatively long pulse duration of 3–6 µs, the resulted spatial resolution is considerably low (few millimeters). The initial electron-induced acoustic pressure $p_0(r)$ (in Pa) is related to the dose deposited as:

$$p_0(\mathrm{r}) = \Gamma \eta_{th} \rho D_r(r) \qquad\qquad (4)$$

where Γ is the Grüneisen coefficient defined as:

$$\Gamma = \frac{\beta K_T}{C_v \rho}, \qquad\qquad \textbf{(5)}$$

which is a dimensionless material-specific constant that relates the pressure increase to the deposited heat energy, rate of change in the deposited dose.

The theory of iRAI and the simulation platform for investigating the applicability of iRAI as a relative dosimetry tool in UHDR-RT is summarized in Figure 1.

Figure 1: Flowchart summarizing the theory and the simulation steps for iRAI and the generation of acoustic images.

B. **Simulation workflow for dose reconstruction**

1. **Dosimetry**

To measure the output of the modified linac (dose rate and dose-per-pulse) delivering in UHDR mode, a full 3D relative dose distribution of the electron field was simulated using Monte Carlo simulation codes EGSnrc Beamnrc/DOSXYZnrc [26,27]. The relative dosimetry simulated results, beam profiles, and percent depth dose (PDD) curves, were compared and verified with film (Gafchromic EBT-XD) measured results at different irradiation positions.

1.1 **Monte Carlo Simulations**

A full model of a 6 MeV electron beam of a 21EX Varian Clinac (Varian Medical Systems, Palo Alto, Ca) modified as part of its decommissioning was used to investigate the dose rates as shown in Figure 2. The initial electron source was modeled with the linac target, flattening filter, and scattering foil removed from the conventional 21EX linac structure to mimic the experimental setup that enables

UHDR-RT dose rates at source-axis distance (SAD)=100 cm, where the acoustic iRAI measurement was performed. Although this setup was irreversible in comparison to the setup reported in the literature, it removed the space constraints of having to conduct experiments in the linac head [9]. A 1x1 cm^2 secondary lead collimator was positioned at 100 cm Source to Surface Distance (SSD) to shape the electron beam incident on a gelatin phantom. The linac phase-space source files were generated using EGSnrc/BEAMnrc. The different components of the linac head were modeled including the initial electron source, ionization chamber, mirror, jaws, and the secondary lead collimation for phase-space generation at the exit of the primary collimation. Full 3D dose simulations were performed in a 30x30x30 cm^3 water tank mimicking the gelatin phantom using EGSnrc/DOSXYZnrc code. For simplicity, the initial electron source was modeled as a monoenergetic 6 MeV pencil beam with a 3 mm 1σ focal spot size. The number of histories used for BEAMnrc was 7×10^8, the photon and electron cut-off energies were set to 100 keV (PCUT) and 521 keV (ECUT), respectively.

The beam characteristics of the 1x1 cm^2 collimated high dose field were investigated for a 6 MeV beam and measured in the water phantom at 10 cm from the secondary lead collimator to mimic the experimental measurements performed with EBT-XD Gafchromic films.

Figure 2: Head structure of the modified 6 MeV 21EX Varian Clinac (This figure is not to scale.) Electrons of monoenergetic 6 MeV pencil beam with a 3 mm 1σ focal spot size pass through the exit window. The resultant electron beam is collimated to the desired field shape by jaws. Further beam collimation is obtained using the manually inserted lead collimators at 100 cm SSD.

1.2 Film measurement

The simulated Monte Carlo dose values and relative dosimetry characteristics of the machine were compared to Gafchromic EBT-XD (Ashland Advanced Materials) film measurements of the dose

distribution. The percent depth dose (PDD) curve was determined at 2 mm x 2 mm region of interest at the central axis of the beam at each irradiation position. Films were placed perpendicular to the beam direction at different depths with 2 mm increments of a solid water phantom along the beam direction. The measured dose per pulse was determined by dividing the film measured dose by the known number of pulses acquired during the specified timeframe. Similarly, the simulated dose per pulse was determined by dividing the dose rate by the number of pulses emitted per second (pulse repetition rate of the linac). A detailed description of the experimental setup was published previously [24].

2. The initial pressure source definition

The irradiation layout considered in the acoustic simulations is shown in Figure 3 where the dose absorbing material used in this study is made of porcine gelatin (10 g/100 ml, G2500, Sigma-Aldrich). A series of CT images of the phantom were acquired and used to determine the material specifications for the acoustic simulation mimicking the experimental setup. According to the electron density of the homogeneous phantom, it was designed to be equivalent to brain tissue as listed in Table 1 [28]. The initial pressure source was defined using the pressure-dose relation (Eq. 4), with a 0.22 Grüneisen coefficient based on the CT number of the gelatin phantom [29].

Table 1: The material characteristics of the gelatin phantom

* y is a frequency dependent exponent of the acoustic attenuation power law. It is a real non-negative material dependent parameter that ranges from 0 to 2.

3. Acoustic propagation K-Wave Simulations

The MATLAB *K*-Wave toolbox [30] was used to simulate electron-induced acoustic wave generation, propagation, and attenuation in the homogeneous gelatin phantom based on its acoustic characteristics to numerically solve the thermoacoustic equation (Eq. 3).

4. The time-reversal reconstruction of initial pressure

Because the instantaneous pressure is received at the ideal transducer positions, the goal of image reconstruction is to recover the initial radiation beam properties, dose, and spatial distribution of the beam, by finding the initial pressure $p_0(r)$ from the instantaneous pressure measurements p(r, t). One of the most common image reconstruction algorithms to recover the initial pressure is using the time-reversal technique.

The time-reversal algorithm can accurately include the effects of heterogeneities in the reconstruction using the appropriate model. Hence, it is more efficient for measuring broadband response and provides a better representation of the physical experiment. However, it is a computationally expensive and time-consuming reconstruction algorithm that could take few hours depending on the simulated geometry [31–33] [30]. The time-reversal reconstruction of the initial pressure in this study was performed using the MATLAB *K*-Wave toolbox [30].

This simulation work covers two different cases with each tested through different transducer (detection) distributions: (A) IRAI measurements of UHDR with default linac operation and (B) Effect of the linac operating parameters on IRAI of UHDR.

A. IRAI measurements of UHDR with clincal linac timing: For these simulations, the linac parameters including the pulse repetition rate and the linac pulse were set to the default values of the linac tested in this study, which were 300 Hz and 4 µs. To demonstrate the imaging capability in the operational mode, two separate distributions of ideal point receiver transducers were used

to run the K-wave simulations in 3-D: a 2D planar matrix array, and a 3D spherical shell distribution around the target.

A.1. Planar transducer distributions:

As shown in Figure 3, the ideal point transducers were placed from the front to the back of the gelatin phantom along a line parallel to and 10 cm away from the beam's central axis. A set of detection points was used to scan the pressure signals along the electron beam path through the phantom up to 3 cm depth with a step size of 2 mm as indicated in Figure 3 a. This setup was used to mimic the experimental setup that was used with a single element transducer for acquiring the PDD curve as shown in Figure 3 b of a published work [24]. A full distribution in a traverse plane with 2 mm increments was used in the simulation for adequate data sampling and collection. A time-reversal reconstruction of the initial pressure source was used to 3D reconstruct the initial dose spatial distribution and determine the relative dosimetric characteristics of the beam.

Figure 3: Schematic setup for simulating the acoustic dose depth measurement. (a) Schematic plot of the setup along the radiation beam direction. (b) Schematic plot of the radiation beam eye view setup. The simulation setup of the planar transducer distribution for 3D dose is using the same setup as in the previously published work [24] assuming a point transducer at each detection point.

A.2. Spherical transducer distributions:

For a better reconstruction using full 3D spatial projections of data, the ideal transducers were simulated to surround the field in a spherical distribution of 600 element transducers evenly distributed over a spherical shell of 2.8 cm radius.

A time-reversal reconstruction of the initial pressure source was then used to 3D reconstruct the initial dose spatial distribution and determine the relative dosimetric characteristic of the beam.

B. The Effect of the linac operating parameters on the induced acoustic signal case:

Clinical linacs deliver radiation as a train of pulses. The typical pulse length is usually on the order of 3–6 μs and a typical pulse repetition frequency ranges from tens to hundreds of hertz (Hz). Each linac pulse is theoretically delivering the same amount of radiation dose. The overall dose rate in many clinical accelerators is varied by varying the pulse repetition rate [34]. The effect of the linac parameters was tested on the induced acoustic signal intensity and the ability in defining the spatial distribution of the initial pressure and hence the radiation beam. Simulation study of the spatial beam profile at the phantom was performed to test the effect of the operational parameters on the overall induced signal. The linac has an approximate pulse duration of 4 μs and a pulse repetition rate of 300 Hz. Two separate studies were performed:

B.1.   The effect of the pulse repetition rate (Linac frequency): By varying pulse repetition frequency of the linac, dose per pulse, is tested for a constant pulse duration of 4 μs. This study was performed using a 2D circular configuration of the ideal point receiver transducers. Ideal transducer points were distributed in a circular configuration that surrounds the beam field and a time-reversal algorithm was used to reconstruct the spatial distribution of the initial pressure from the instantaneous pressure signal for both cases (Figure 4). A grid size of 0.06 mm was used for all the simulations to allow for acceptable temporal resolution within a simulation time interval of 54 μs.

Figure 4: The Beam's-eye-view diagram of the 2D set-up used for simulating the linac parameters effect. A circular distribution of the ideal point transducers of constant distance from the beam center. Transducers were distributed in a water tank irradiated with a linac electron beam of 1x1 cm² field size.

B.2. **The effect of the linac pulse duration**, the pulse duration and instantaneous dose per pulse effects were tested for different linac pulse durations at a constant linac pulse repetition frequency of 300 Hz. This study was performed using two different transducer distributions.

1. *2D circular configuration of the ideal point receiver transducer*s: using the same parameters and setup as in the effect of the pulse frequency case (Figure 4).

2. *Spherical transducer distribution:* using the same distribution mentioned in section A.2 for a better reconstruction using full 3D spatial projections of data. This simulation is done to test the effect of the linac pulse duration on the overall spatial distribution of the acquired pressure-based beam characteristic in the ideal case of a full data collection through point transducer elements with no bandwidth limitations and distributed on the surface of a spherical shell.

Results

1. Field characteristics and relative dose measurements

The full 3D dosimetric spatial distribution of the iRAI electron beam was scored through EGSnrc Monte Carlo code. The resulting dose was reported as the dose per linac pulse given a constant pulse repetition rate of the linac of 300 Hz, as shown in Figure 5. The relative dosimetry data, both PDD curves, and beam profiles (Figure 6) were extracted and validated with the experimental film dose results. Monte Carlo-based PDD simulated at the central beam region of 5x5 mm^2 in the water phantom agreed with the film measured PDD within less than 6 % relative error for depths less than 2 cm. The inherent statistical uncertainty in the simulated PDD was < 1.3%. Similarly, the simulated and the measured film profiles agreed to ≤5% relative error between the two methods at all points within the central region of the radiation beam.

Figure 5: The 3D simulated dose distribution in phantom using EGSnrc Monte Carlo code. a): XY plane (cross beam plane) at the surface of the phantom (at 0 cm depth), b): ZX plane (along

beam plane) scored at beam center (y=0 cm), c): ZY plane scored at beam center (x=0 cm). Showing the expected tear drop distribution of the electron beam dose in water.

Figure 6: The simulated relative dosimetry characteristics of the electron beam compared to the Gafchromic EBT-XD film measurement. a) The beam profiles at various depths in the water phantom normalized at the central axis. Showing the increase in the field size (FWHM) with depth. b) PDD curve showing both film measurement and simulation results. Simulation PDD results were extracted at the central 5x5 mm^2 region of the water phantom to decrease the simulation uncertainty, while the film results were extracted over the central 2x2 mm^2.

The initial pressure source spatial distribution (Figure 7) was defined based on the dose-pressure proportionality (Eq. 4) and defined in the dose per pulse basis using the 0.22 Grüneisen coefficient for the gelatin phantom.

Figure 7: The simulated 3D spatial initial pressure source distribution in the gelatin phantom, defined using the acoustic properties listed in Table 1. a): XY plane (cross beam plane) at the surface of the phantom (at 0 cm depth), b): ZX plane (along beam plane) scored at beam center (y=0 cm), c: ZY plane scored at beam center (x=0 cm), showing the similarity of this simulated spatial initial pressure distribution to that of the electron dose distribution in water.

A. Linac operational case:

A.1. The planar transducer distribution case

The instantaneous pressure signal indicates the edges of the beam based on the central region of the pressure change (Figure 8 a). The temporal change in pressure is converted to distance based on the speed of sound of the medium and hence defining the FWHM of the beam. The agreement between the beam size (FWHM) defined with the simulated dose profiles and those extracted with the instantaneous pressure signal is within 3 mm at the surface of the phantom, and increases with depth due to the contribution of the linac pulse duration effect.

The time-reversal reconstructed pressure-based percent curve was compared to the Monte Carlo calculated PDD curve as shown in Figure 8 b. The disagreement between the two curves is as high as 11% for the surface dose and within ~ 7% for up to 1 cm depth region beyond which the relative error increases with depth. This error is related to the reconstruction algorithm mainly due to the linac pulse duration effect, the limited detection view, and incomplete data measurements which inherently contribute to the error. Correction of the linac pulse duration effect through signal processing (deconvolution) increases the agreement between the two curves for the depths between 5 mm to 2 cm such that the maximum disagreement between the two curves is within ~ 7% relative percent error. The surface and the endpoint signals are highly affected with the limited detection view artifact.

Figure 8: Simulated pressure signal measured by a point transducer at the side of the phantom 10 cm away from the beam center. a): shows the conversion of the instantaneous pressure signal arrival in terms of the distance, compared to the dose profile simulated by EGSnrc Monte Carlo code and the film measured profile. The offset of the pressure signal relative to the beam profile is due to the effect of the linac pulse duration. b) shows the iRAI based PDD equivalent curve retrieved along the central axis of the beam based on the 3D time-reversal reconstruction of the

iRAI initial pressure source from iRAI simulation compared to the PDD simulated by Monte Carlo code EGSnrc.

A.2. The spherical transducer distribution case

The instantaneous pressure signal analysis was performed using a full, 3D spherical distribution of point transducers to get the relative characteristics of the beam. The 3D pressure signal-based reconstructed beam profiles and the pressure equivalent PDD were compared to the Monte Carlo simulated relative dosimetric beam characteristics as shown in Figure 9.

The TR reconstructed pressure-based percent curve was compared to the Monte Carlo based PDD curve as shown in Figure 9 a. The superficial (~ 4 mm) pressure based curve underestimated the signal by as high as 46% relative to the percent dose curve, and up to 1 cm depth, the two curves agree within ~ 7%. The sharp surface increase in the signal near the buildup region is correctible through signal processing as discussed previously, as it is due to the predictable geometrical reconstruction artifact of the linac pulse duration which reflects the accumulation of the signal during the pulse duration. The relative error increases with depth due to the linac pulse duration effect to as high as 100% near the distal position corresponding to the maximum electron range. A correction of the pulse duration effect through linac pulse deconvolution (Figure 9 a) has resulted in better agreement for EGSnrc PDD and the pressure-based percent depth curves normalized to the 1 cm depth. The maximum relative percent disagreement for depths 1 mm to 2 cm was within 8%.

The reconstructed pressure profile has a wider beam size (FWHM) than the relevant Monte Carlo simulated dose beam profiles (within 4 mm) due to the inherent effect of the linac pulse duration which affects the spatial resolution of the reconstructed pressure profiles as shown in Figure 9 b.

Figure 9: the results of the relative 3D TR reconstructed pressure signal-based beam characteristics measured by 3D spherical point transducer distribution (radius =2.8 cm away from the beam center). a) shows the iRAI based PDD equivalent curve normalized at 1 cm depth retrieved based on the 3D time-reversal reconstruction of the iRAI initial pressure source from iRAI acoustic simulation with and without the correction of the linac pulse duration compared to the dose-based PDD simulated by Monte Carlo code EGSnrc. b) shows the iRAI based beam profiles retrieved based on the 3D time-reversal reconstruction of the iRAI initial pressure compared to the dose profiles simulated by Monte Carlo code EGSnrc.

B. The Effect of the linac operating parameters on the induced acoustic signal case:

B.1. The effect of the pulse repetition rate (Linac frequency): The temporal average dose rate of the simulated linac was set to be constant of 84 Gy/s as the pulse repetition rate (frequency) was varied, thus producing a dose per pulse inversely proportional to the pulse repetition rate. The induced acoustic signal is inversely proportional to the linac pulse repetition frequency (Figure 10 a), and linearly with dose per pulse. The Root Mean Square Error (RMSE) between the dose per pulse and the maximum instantaneous pressure signal is 0.027. Additionally, R^2 is nearly unity, as shown in Figure 10 b, reflecting the linear proportionality of the induced acoustic signal to the linac dose per pulse as predicted theoretically.

Figure 10: The effect of the linac pulse repetition rate in the acoustic signal and dose per pulse assuming a constant linac dose rate per pulse. a): the effect of changing the linac pulse repetition rate (linac frequency), while maintaining the same pulse duration time of 4μs. The dose is

related to the pressure signal through the phantom-dependent proportionality factor. b): showing the linearity of the linac dose per pulse and the induced acoustic signal intensity.

B.2. The effect of the linac pulse duration:

1. *2D circular configuration of the ideal point receiver transducers*

The temporal average dose rate of the simulated linac was set to be constant as pulse duration was varied hence varying the instantaneous dose rate during the pulse. The induced acoustic signal amplitude decreases with increasing the linac pulse duration, which defines the instantaneous dose rate during the pulse as shown in Figure 11 for pulse durations of 0.6 µs length and longer. The effect of the pulse duration on the 2D TR reconstructed images of the initial pressure source, extracted at the phantom entrance (zero depth), is shown in Figure 12 and the quantitative gamma test comparison results are listed in Table 2. Both the increased gamma-test pass-rate, and the qualitatively good image resolution at the shorter pulse durations of the linac, indicate the direct relation between the linac pulse duration and the temporal (spatial) resolution of iRAI. The FWHM of the TR reconstructed beam (Figure 13) agrees within 2% relative error to the dose beam profile for linac pulse durations that are less than 1 µs and increase to 15.4% and 39.8% for the larger linac pulse durations of 4 µs and 6 µs, respectively.

Figure 11: The effect of the linac pulse duration time in the induced acoustic signal and instantaneous dose during pulse assuming a constant linac dose per pulse (constant frequency of 300 Hz).

Figure 12: Time-reversal 2D reconstructed initial pressure source at the phantom entrance for different initial linac pulse duration time. a) initial spatial pressure distribution assuming a) a

delta function linac pulse, b) at 0.1 μs, c) 0.4 μs, d) 1 μs, e) 4 μs, f) 6 μs. Showing the effect of the linac pulse duration in spatial resolution and the efficiency in determining the radiation beam edges (source edges), showing the noticeable beam size increase for the 4 μs and 6 μs pulse duration cases.

Table 2: Percent of points in the reconstructed image passing Gamma test criteria between the reconstructed spatial pressure distribution and the relative dose distribution levels for the five different linac pulse durations.

Figure 13: The effect of the pulse duration of the linac on spatial fidelity of the signal as shown by the horizontal beam profiles at the phantom entrance (zero depth) for the time-reversal 2D reconstructed initial pressure source compared to the horizontal beam profile.

2. *Spherical transducer distribution:*

Similarly, the 3D effect of the linac pulse duration, duration of the dose deposition, affects the spatial fidelity of the reconstructed initial spatial pressure. The longer the pulse duration, the worse the spatial fidelity of the reconstructed 3D images in the different planes of the initial radiation beam. The gamma test results for 3%/3mm criteria are 99.9%, 99.4%, and 92.5% for 1 μs, 4 μs, and 6 μs linac pulse durations respectively. While for the 1mm/1% gamma test, the passing rate of the pixels is 98.9%, 91.5%, and 86.2% respectively. Hence, the edges of the radiation beam are defined more accurately using TR reconstruction of the instantaneous measured acoustic pressure signals as the linac pulse duration decreases. As shown in Figure 14 a, the effect of the linac pulse resolution affects the reconstructed pressure-based percent curve such that the longer the pulse, the steeper the pressure percent curve.

A signal processing deconvolution technique was implemented to correct for this effect. The deconvolution of the temporal signal of the linac pulse duration has resulted in a better agreement between EGSnrc and the 3D reconstructed iRAI results. With the deconvolution signal processing correction, the gamma test results for 3%/3mm criteria has increased to 99.9% for all the tested linac pulse durations. While for the 1mm/1% gamma test, the passing rate of the pixels is 98.4%, 98.7%, and 98.7% for 1 µs, 4 µs, and 6 µs linac pulse durations respectively.

The shift in the buildup region of the pressure-based percent curve is a geometrical artifact caused by the relatively long linac pulse duration. The PDD and the corrected pressure-based percent depth curves normalized to the 1 cm depth signal for the different linac pulse duration times are shown in Figure 14 b. With the deconvolution signal processing correction, the PDD and the corrected pressure-based percent depth curves agree for depths from 1 mm to 2 cm within 8% relative error for the 4 µs and 6 µs pulse durations. For the 1 µs case, the maximum relative error was within 11%.

Figure 14: a) The reconstructed pressure-based percent depth curve for the different linac pulse durations relative to the Monte Carlo-based PDD curve. b) The reconstructed pressure-based percent depth curve normalized to the 1 cm depth signal for the different linac pulse durations corrected for the pulse duration shift with temporal linac pulse deconvolution and compared relative to the Monte Carlo-based PDD curve.

Discussion

The dosimetric feasibility of iRAI was tested through simulation studies. The simulation results were compared to the EGSnrc MC dose deposition for an electron beam that was commissioned with film measurements as shown in Figure 6. The maximum point percent dose difference between the film and simulated PDD curve results was as high as 66% at the end of the particle track (3 cm depth) as shown in Figure 6 b. The relative error increased with depth due to the increased simulation uncertainty with the reduction of the particles at the end of the particle track where the vast majority of the simulated particles stop. The relatively small disagreement between the simulated MC based and the measured PDD specifically at the buildup region could be caused by the MC initial electron source differences, where for simplicity we used a monoenergetic beam. The initial electron source parameters, specifically the electron beam energy distribution (mean energy), were not validated and calibrated due to limited experimental calibration data at the modified machine setting. The agreement between the simulations and the film measurements specifically at depths less than 2 cm depth is within ~6% maximum relative point error. However, it is recommended to do a full beam tuning to even better improve the agreement between the simulated and the measured PDD curves.

The beam profiles of the Monte Carlo simulations, specifically for depths less than 2 cm, and the film measured profiles agreed within a ≤5% relative error for the central region of the radiation beam (Figure 6 a). The simulated beam profile sizes expressed in FWHM were in agreement with the measured FWHM within 1 mm. Hence, per the relative dosimetry comparisons, the full 3D distribution of the dose in the phantom was predicted within < 6% relative percent error, specifically at the expected therapeutic depth of 2 cm for this electron beam.

The effect of the pulse duration on the acoustical signal was in good agreement with results published in the literature. The shorter the linac pulse the higher the instantaneous maximum acoustical signal given a constant dose rate and pulse repetition frequency [12]. The iRAI based FWHM of the 1x1 cm^2 profiles, produced with the 2D time-reversal reconstruction of the iRAI images, was highly affected by the tested linac pulse durations. For the 4 μs linac case, the FWHM of the iRAI profile was within approximately 2 mm in comparison to the Monte Carlo simulated dose spatial FWHM of the field (Figure 13). This 2 mm beam size based resolution is in reasonable agreement with the result

published in literature testing the XACT 2D dose reconstruction versus film measurement for a 4 mm diameter stereotactic cone field that has reported to have FWHM of 6 mm resolution of the implementation of XACT in the study [35].

Due to the effect of the linac pulse duration, the reconstructed planar percent depth pressure curve is steeper than the PDD curve (Figure 8 b). This is a combination of different effects; the long linac pulse duration, limited detection view, and incomplete data measurements. At shallower depths closer to the beam entrance, the FWHM of the beam was simulated through single element transducer measurement of the instantaneous pressure is within 3 mm relative to the MC based FWHM. At deeper depths, the contributions of linac pulse duration effect cause degradation of the beam edges allocation to be within 26% relative error.

The considerably long linac pulse duration, which strongly affects the spatial resolution and hence the reconstructed beam characteristics including beam profiles and the depth curve. Correction of the linac pulse duration effect through signal processing (deconvolution) increases the agreement between the two curves for the depths between 5 mm to 2 cm such that the maximum disagreement between the two curves is within ~ 7% relative error. The endpoint signals are highly affected with the limited detection view artifact.

The 3D time-reversal reconstruction part of this work is conducted to test the effect of the linac pulse duration on the overall spatial distribution of the acquired pressure-based beam characteristic in the ideal case of a full data collection through point transducer elements with no bandwidth limitations and distributed on a spherical shell. Realistic limitations can be evaluated in specific cases. Limitations on practically available transducer configurations allowing access of the ionizing radiation beam path between, presumably fixed, transducer elements, will reduce the sensitivity, spatial resolution and fidelity, of the reconstructed images. With careful aperture configuration and image reconstruction, effects of these limitations can be reduced substantially. Future work could implement an iterative reconstruction approach which was found to eliminate data sparsity specifically at the phantom entrance (beam entrance) [36]. Further experiments with multiple projections

would better reconstruct the full 3D dose distribution and fully define the spatial 3D beam characteristics. For example, ultrasound reception could be performed with crossed linear arrays, one normal to and one parallel to the beam central axis. Additionally, a hemispherical transducer array will work well in predicting the full spherical distribution of the pressure-based beam characteristics due to the 3D nature of the collected acoustical signals.

The main challenge for iRAI implementation for dosimetry as shown in the results of this study is the relatively long pulse duration length for the clinical linacs. This effect needs to be addressed because it strongly affects the resolution of the reconstructed images and hence the relative dosimetry characteristics. The approach used to resolve this issue is to implement signal processing techniques, i.e., deconvolution of the instantaneous pressure signals for the linac pulse shape before implementing the image reconstruction algorithm. The deconvolution has improved the quality of the reconstructed pressure images and hence the beam characterization. As per the results of this study, the maximum disagreement for depths 1 mm to 2 cm for the clinical linac pulse duration of 4 µs was within 8% relative error. Achieving this accuracy elsewhere will depend on the transducer placement.

The results in this paper are testing the implementation of iRAI in UHDR-RT showing that for high instantaneous dose rates used in UHDR, even at the highest UHDR's in the literature, the resulting acoustic pressures are far from causing nonlinear acoustic propagation as reported in this study. In addition, those high dose rates will result in much better acoustical signal to noise ratio in comparison to the current signal of this work.

Conclusions

A full simulation study was conducted in a homogenous phantom to test the feasibility of iRAI for UHDR-RT. The configuration of the 3D iRAI imaging capability and acoustical signal generation was simulated assuming a distribution of ideal transducer elements over a sphere to optimize 3D volumetric imaging capabilities. Transducers with finite bandwidths and practical dimensions must be considered next.

IRAI has shown the advantage of 3D dose mapping through the dose signal linearity demonstrating its potential as an in-vivo relative dosimetry tool for UHDR-RT. The limited spatial resolution (few millimeters) due to the inherent linac pulse duration effect can be improved through linac pulse deconvolution, which has improved the agreement between the pressure-constructed and dosimetric beam characteristic to be within a 98% passing rate for 1%/1mm gamma test criteria. Because UHDR-RT is delivering a higher instantaneous dose per pulse, it enforces the need for and value of instantaneous dose measurements such as iRAI for patient safety. A dedicated machine that delivers UHDR-RT could has the advantage of improving the SNR of iRAI and allowing faster treatment delivery.

Conflict of interest

The authors have no conflicts to disclose.

Data availability:

The data that support the findings of this study are available from the corresponding author upon reasonable request.

References:

1.   Lempart M, Blad B, Adrian G, et al. Modifying a clinical linear accelerator for delivery of ultra-high dose rate irradiation. Radiotherapy and Oncology. 2019;139:40-45. doi:10.1016/j.radonc.2019.01.031

2.   Favaudon V, Caplier L, Monceau V, et al. Erratum: Ultrahigh dose-rate FLASH irradiation increases the differential response between normal and tumor tissue in mice (Science Translational Medicine DOI: 10.1126/scitranslmed.3008973). Science Translational Medicine. 2019;11(523):1-10. doi:10.1126/scitranslmed.aba4525

3.   Montay-Gruel P, Bouchet A, Jaccard M, et al. X-rays can trigger the FLASH effect: Ultra-high dose-rate synchrotron light source prevents normal brain injury after whole brain irradiation in mice. Radiotherapy and Oncology. 2018;129(3):582-588. doi:10.1016/j.radonc.2018.08.016

4.   Simmons DA, Lartey FM, Schüler E, et al. Reduced cognitive deficits after FLASH irradiation of whole mouse brain are associated with less hippocampal dendritic spine loss and neuroinflammation. Radiotherapy and Oncology. 2019;139:4-10. doi:10.1016/j.radonc.2019.06.006

5.   Vozenin MC, De Fornel P, Petersson K, et al. The Advantage of FLASH Radiotherapy Confirmed in Mini-pig and Cat-cancer Patients. Clinical Cancer Research. 2019;25(1):35-42. doi:10.1158/1078-0432.CCR-17-3375

6. Montay-Gruel P, Petersson K, Jaccard M, et al. Irradiation in a flash: Unique sparing of memory in mice after whole brain irradiation with dose rates above 100 Gy/s. Radiotherapy and Oncology. 2017;124(3):365-369. doi:10.1016/j.radonc.2017.05.003

7. Lohse I, Lang S, Hrbacek J, et al. Effect of high dose per pulse flattening filter-free beams on cancer cell survival. Radiotherapy and Oncology. 2011;101(1):226-232. doi:10.1016/j.radonc.2011.05.072

8. Bourhis J, Sozzi WJ, Jorge PG, et al. Treatment of a first patient with FLASH-radiotherapy. Radiotherapy and Oncology. 2019;139:18-22. doi:10.1016/j.radonc.2019.06.019

9. Schüler E, Trovati S, King G, et al. Experimental Platform for Ultra-high Dose Rate FLASH Irradiation of Small Animals Using a Clinical Linear Accelerator. International Journal of Radiation Oncology Biology Physics. 2017;97(1):195-203. doi:10.1016/j.ijrobp.2016.09.018

10. di Martino F, Barca P, Barone S, et al. FLASH Radiotherapy With Electrons: Issues Related to the Production, Monitoring, and Dosimetric Characterization of the Beam. Frontiers in Physics. 2020;8. doi:10.3389/fphy.2020.570697

11. Li Y, Samant P, Wang S, Behrooz A, Li D, Xiang L. 3-D X-Ray-Induced Acoustic Computed Tomography with a Spherical Array: A Simulation Study on Bone Imaging. IEEE Transactions on Ultrasonics, Ferroelectrics, and Frequency Control. 2020;67(8):1613-1619. doi:10.1109/TUFFC.2020.2983732

12. Xiang L, Tang S, Ahmad M, Xing L. High Resolution X-ray-Induced Acoustic Tomography. Scientific Reports. 2016;6:2-7. doi:10.1038/srep26118

13. Hickling S, Xiang L, Jones KC, et al. Ionizing radiation-induced acoustics for radiotherapy and diagnostic radiology applications. Medical Physics. 2018;45(7):e707-e721. doi:10.1002/mp.12929

14.   Xiang L, Han B, Carpenter C, Pratx G, Kuang Y, Xing L. X-ray induced photoacoustic tomography. Photons Plus Ultrasound: Imaging and Sensing 2013. 2013;8581(March 2013):85811I. doi:10.1117/12.2005765

15.   Lei H, Zhang W, Oraiqat I, et al. Toward in vivo dosimetry in external beam radiotherapy using x-ray acoustic computed tomography: A soft-tissue phantom study validation. Medical Physics. 2018;45(9):4191-4200. doi:10.1002/mp.13070

16.   Xiang L, Han B, Carpenter C, Pratx G, Kuang Y, Xing L. X-ray acoustic computed tomography with pulsed x-ray beam from a medical linear accelerator. Medical Physics. 2013;40(1):1-5. doi:10.1118/1.4771935

17.   Hickling S, Lei H, Hobson M, Léger P, Wang X, El Naqa I. Experimental evaluation of x-ray acoustic computed tomography for radiotherapy dosimetry applications. Medical Physics. 2017;44(2):608-617. doi:10.1002/mp.12039

18.   Hickling S, Léger P, El Naqa I. On the Detectability of Acoustic Waves Induced Following Irradiation by a Radiotherapy Linear Accelerator. IEEE Transactions on Ultrasonics, Ferroelectrics, and Frequency Control. 2016;63(5):683-690. doi:10.1109/TUFFC.2016.2528960

19.   Sampaio DiRT, Uliana JH, Carneiro AAO, Pavoni JF, Pavan TZ, Borges LF. X-ray acoustic imaging for external beam radiation therapy dosimetry using a commercial ultrasound scanner. In: 2015 IEEE International Ultrasonics Symposium, IUS 2015. ; 2015:15-18. doi:10.1109/ULTSYM.2015.0400

20.   Samant P, Trevisi L, Ji X, Xiang L. X-ray induced acoustic computed tomography. Photoacoustics. 2020;19(March). doi:10.1016/j.pacs.2020.100177

21.   Tang S, Yang K, Chen Y, Xiang L. X-ray-induced acoustic computed tomography for 3D breast imaging: A simulation study. Medical Physics. 2018;45(4):1662-1672. doi:10.1002/mp.12829

22.   Choi S, Lee D, Park E-Y, Min J-J, Lee C, Kim C. 3D x-ray induced acoustic computed tomography: a phantom study. 2020;(February):168. doi:10.1117/12.2543673

23.   Zhang W, Oraiqat I, Lei H, Carson PL, Naqa IEI, Wang X. Dual-Modality X-Ray-Induced Radiation Acoustic and Ultrasound Imaging for Real-Time Monitoring of Radiotherapy. BME Frontiers. 2020;2020.

24.   Oraiqat I, Zhang W, Litzenberg D, et al. An ionizing radiation acoustic imaging (iRAI) technique for real-time dosimetric measurements for FLASH radiotherapy. Medical Physics. 2020;47(10):5090-5101. doi:10.1002/mp.14358

25.   Ross CK, Klassen N V, Shortt KR, Smith GD. A direct comparison of water calorimetry and Fricke dosimetry. Physics in Medicine & Biology. 1989;34(1):23-42.

26.   Rogers DWO, Walters B, Kawrakow I. BEAMnrc Users Manual. Nrc Report Pirs.; 2009.

27.   Walters B, Kawrakow I, Rogers DWO. DOSXYZnrc Users Manual. Nrc Report Pirs.; 2005.

28.   Szabo TL. DIAGNOSTIC ULTRASOUND IMAGING: INSIDE OUT.; 2004. doi:10.1016/b978-0-12-680145-3.50022-0

29.   Mast TD. Empirical relationships between acoustic parameters in human soft tissues. Acoustic Research Letters Online. 2000;1(November):37-42. doi:10.1121/1.1336896

30.   Treeby BE, Cox BT. k-Wave: MATLAB toolbox for the simulation and reconstruction of photoacoustic wave fields. Journal of Biomedical Optics. 2010;15(2):021314. doi:10.1117/1.3360308

31.   Burgholzer P, Matt GJ, Haltmeier M, Paltauf G. Exact and approximative imaging methods for photoacoustic tomography using an arbitrary detection surface. Physical Review E

-      Statistical,   Nonlinear,   and   Soft   Matter   Physics.   2007;75(4):1-10. doi:10.1103/PhysRevE.75.046706

32.   Xu Y, Wang L V. Time Reversal and Its Application to Tomography with Diffracting Sources. Physical Review Letters. 2004;92(3):4. doi:10.1103/PhysRevLett.92.033902

33.   Hristova Y, Kuchment P, Nguyen L. Reconstruction and time reversal in thermoacoustic tomography in acoustically homogeneous and inhomogeneous media. Inverse Problems. 2008;24(5). doi:10.1088/0266-5611/24/5/055006

34.   IAEA. RADIATION ONCOLOGY PHYSICS: A HANDBOOK FOR TEACHERS AND STUDENTS. Vol 52.; 2005. doi:10.1021/jf030837o

35.   Hickling S, Hobson M, El Naqa I. Characterization of X-Ray Acoustic Computed Tomography for Applications in Radiotherapy Dosimetry. IEEE Transactions on Radiation and Plasma Medical Sciences. 2018;2(4):337-344. doi:10.1109/trpms.2018.2801724

36.   Forghani F, Mahl A, Patton TJ, et al. Simulation of x-ray-induced acoustic imaging for absolute dosimetry: Accuracy of image reconstruction methods. Medical Physics. 2020;47(3):1280-1290. doi:10.1002/mp.13961

Table of figure legend:

Figure 1: Flowchart summarizing the theory and the simulation steps for iRAI and the generation of acoustic images.   8
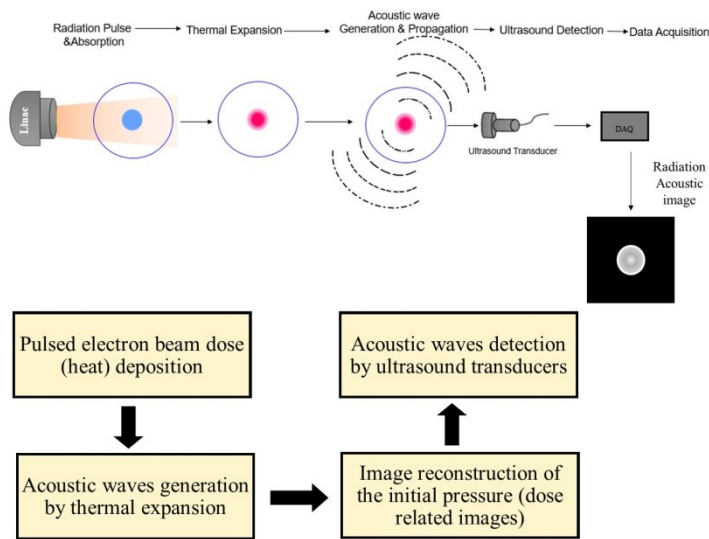
Figure 2: Head structure of the modified 6 MeV 21EX Varian Clinac (This figure is not to scale.) Electrons of monoenergetic 6 MeV pencil beam with a 3 mm 1σ focal spot size pass through the exit window. The resultant electron beam is collimated to the desired field shape by jaws. Further beam collimation is obtained using the manually inserted lead collimators at 100 cm SSD.   9
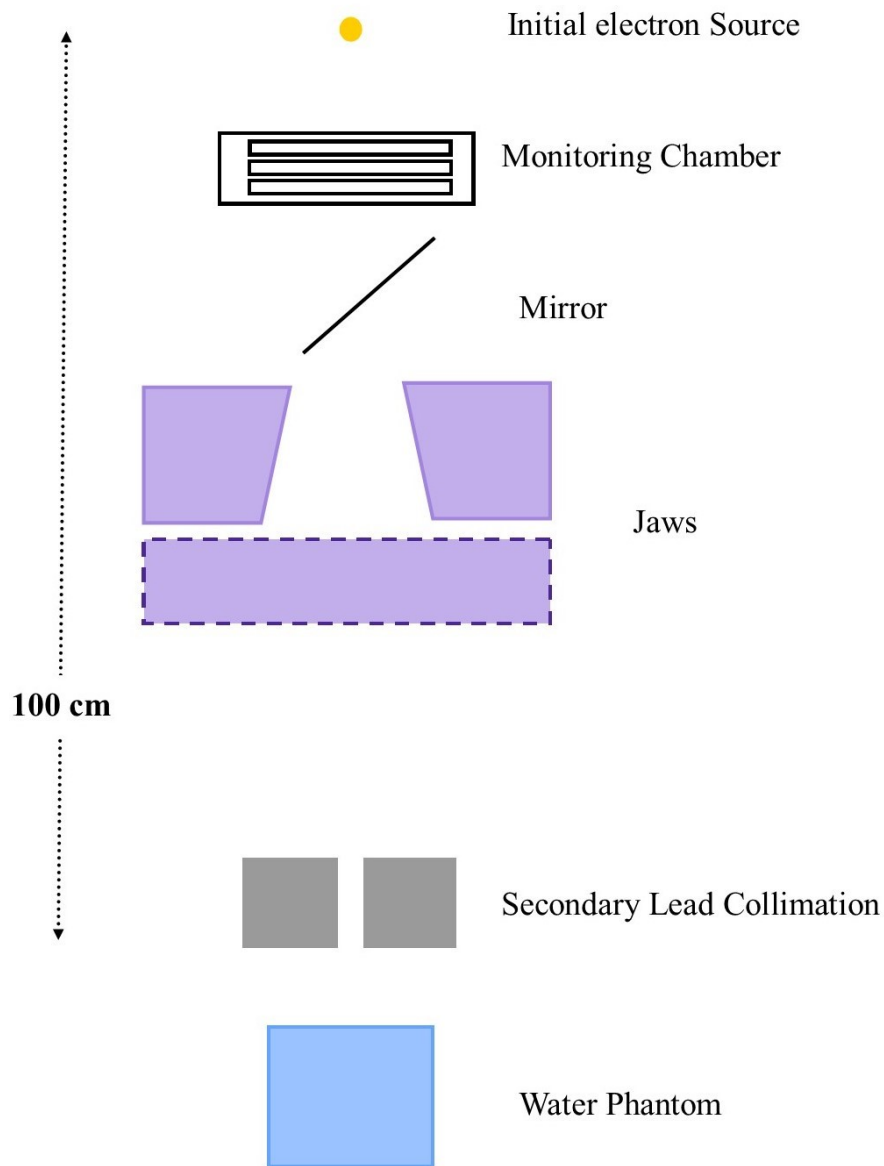
Figure 3: Schematic setup for simulating the acoustic dose depth measurement. (a) Schematic plot of the setup along the radiation beam direction. (b) Schematic plot of the radiation beam eye view setup. The simulation setup of the planar transducer distribution for 3D dose is using the same setup as in the previously published work 24 assuming a point transducer at each detection point. 12
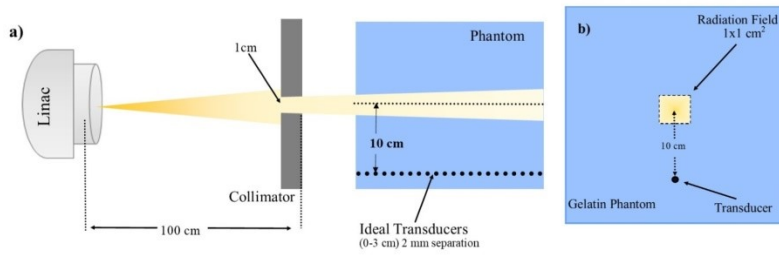
Figure 4: The Beam's-eye-view diagram of the 2D set-up used for simulating the linac parameters effect. A circular distribution of the ideal point transducers of constant distance from the beam center. Transducers were distributed in a water tank irradiated with a linac electron beam of 1x1 cm2 field size. 13
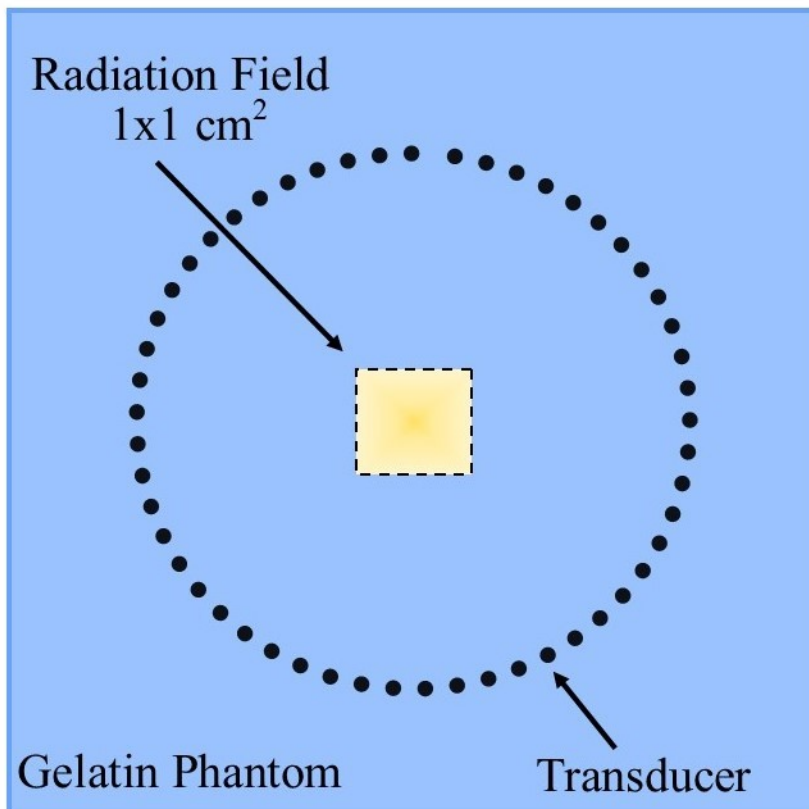
Figure 5: The 3D simulated dose distribution in phantom using EGSnrc Monte Carlo code. a): XY plane (cross beam plane) at the surface of the phantom (at 0 cm depth), b): ZX plane (along beam plane) scored at beam center (y=0 cm), c): ZY plane scored at beam center (x=0 cm). Showing the expected tear drop distribution of the electron beam dose in water. 14
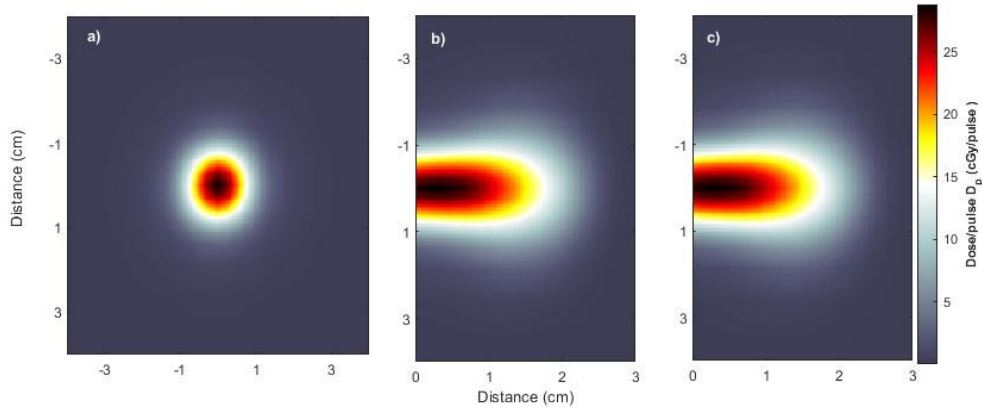
Figure 6: The simulated relative dosimetry characteristics of the electron beam compared to the Gafchromic EBT-XD film measurement. a) The beam profiles at various depths in the water phantom normalized at the central axis. Showing the increase in the field size (FWHM) with depth. b) PDD curve showing both film measurement and simulation results. Simulation PDD results were extracted at the central 5x5 mm2 region of the water phantom to decrease the simulation uncertainty, while the film results were extracted over the central 2x2 mm2. 15

Figure 7: The simulated 3D spatial initial pressure source distribution in the gelatin phantom, defined using the acoustic properties listed in Table 1. a): XY plane (cross beam plane) at the surface of the phantom (at 0 cm depth), b): ZX plane (along beam plane) scored at beam center (y=0 cm), c: ZY plane scored at beam center (x=0 cm), showing the similarity of this simulated spatial initial pressure distribution to that of the electron dose distribution in water.
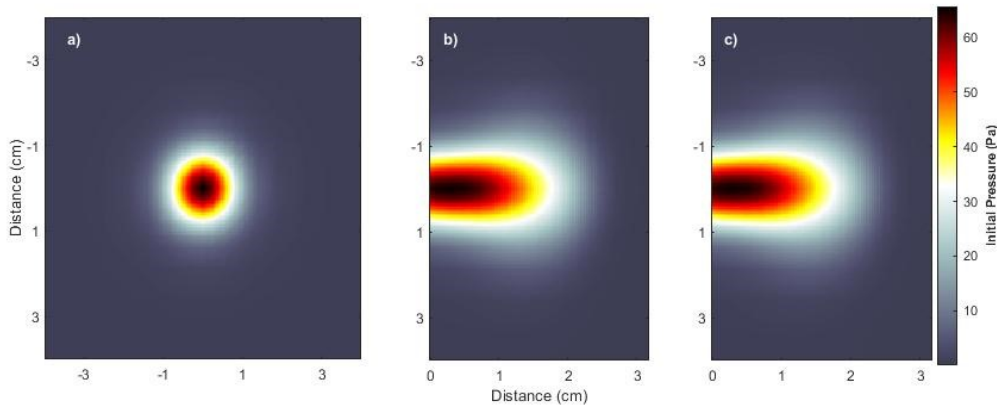
15

Figure 8: Simulated pressure signal measured by a point transducer at the side of the phantom 10 cm away from the beam center. a): shows the conversion of the instantaneous pressure

signal arrival in terms of the distance, compared to the dose profile simulated by EGSnrc Monte Carlo code and the film measured profile. The offset of the pressure signal relative to the beam profile is due to the effect of the linac pulse duration. b) shows the iRAI based PDD equivalent curve retrieved along the central axis of the beam based on the 3D time-reversal reconstruction of the iRAI initial pressure source from iRAI simulation compared to the PDD simulated by Monte Carlo code EGSnrc. 16
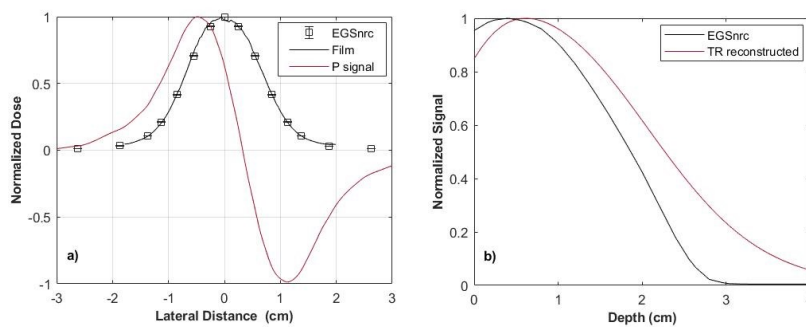

Figure 9: the results of the relative 3D TR reconstructed pressure signal-based beam characteristics measured by 3D spherical point transducer distribution (radius =2.8 cm away from the beam center). a) shows the iRAI based PDD equivalent curve normalized at 1 cm depth retrieved based on the 3D time-reversal reconstruction of the iRAI initial pressure source from iRAI acoustic simulation with and without the correction of the linac pulse duration compared to the dose-based PDD simulated by Monte Carlo code EGSnrc. b) shows the iRAI based beam profiles retrieved based on the 3D time-reversal reconstruction of the iRAI initial pressure compared to the dose profiles simulated by Monte Carlo code EGSnrc.   17
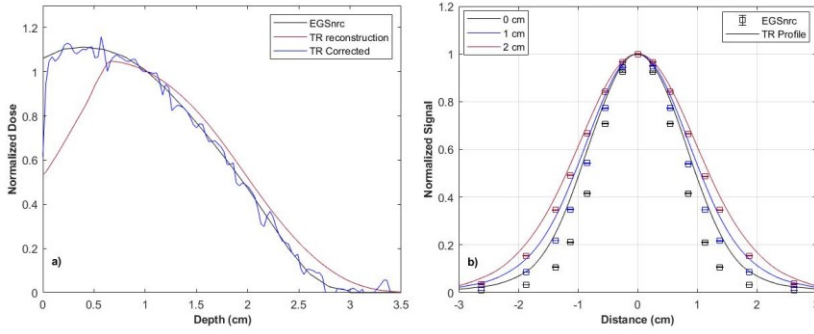
Figure 10: The effect of the linac pulse repetition rate in the acoustic signal and dose per pulse assuming a constant linac dose rate per pulse. a): the effect of changing the linac pulse repetition rate (linac frequency), while maintaining the same pulse duration time of 4µs. The dose is related to the pressure signal through the phantom-dependent proportionality factor. b): showing the linearity of the linac dose per pulse and the induced acoustic signal intensity. 18
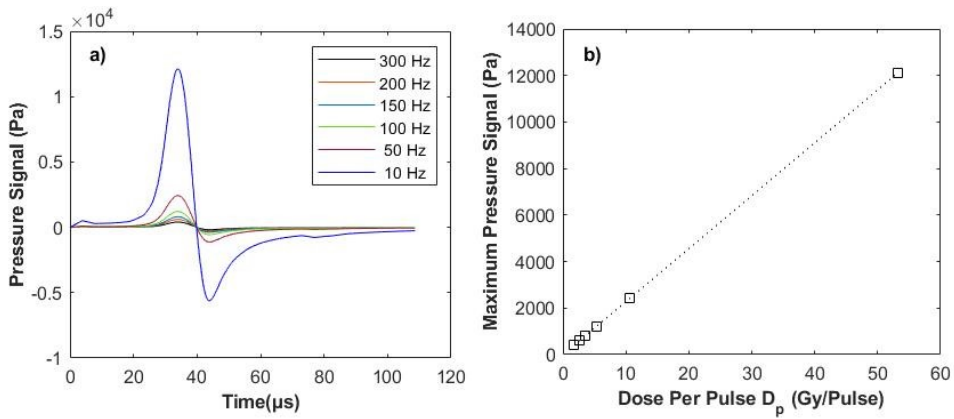

Figure 11: The effect of the linac pulse duration time in the induced acoustic signal and instantaneous dose during pulse assuming a constant linac dose per pulse (constant frequency of 300 Hz).   19
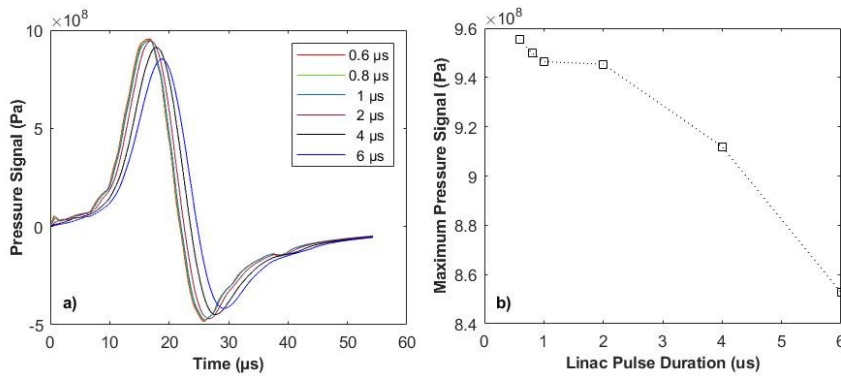
Figure 12: Time-reversal 2D reconstructed initial pressure source at the phantom entrance for different initial linac pulse duration time. a) initial spatial pressure distribution assuming a) a delta function linac pulse, b) at 0.1 µs, c) 0.4 µs, d) 1 µs, e) 4 µs, f) 6 µs. Showing the effect of the linac pulse duration in spatial resolution and the efficiency in determining the radiation beam edges (source edges), showing the noticeable beam size increase for the 4 µs and 6 µs pulse duration cases.   19
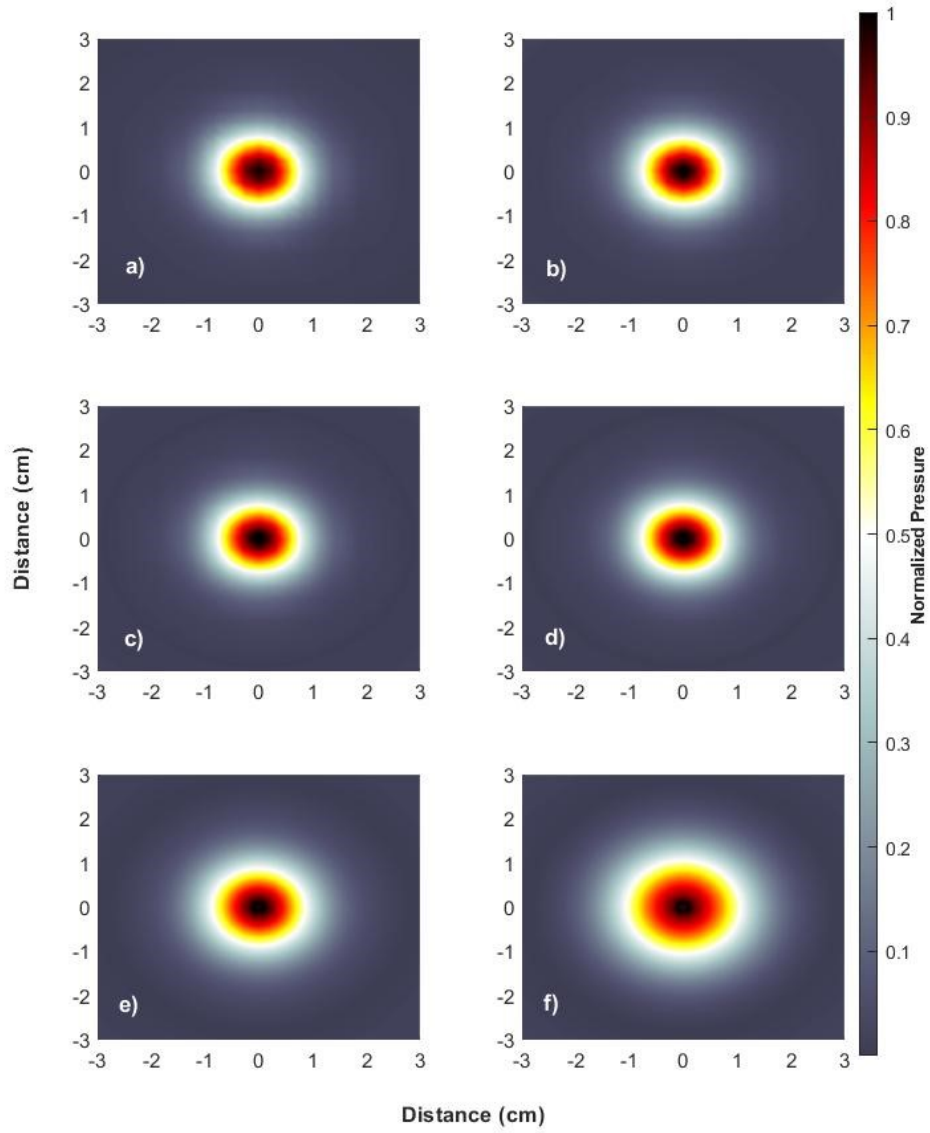
Figure 13: The effect of the pulse duration of the linac on spatial fidelity of the signal as shown by the horizontal beam profiles at the phantom entrance (zero depth) for the time-reversal 2D reconstructed initial pressure source compared to the horizontal beam profile. 20
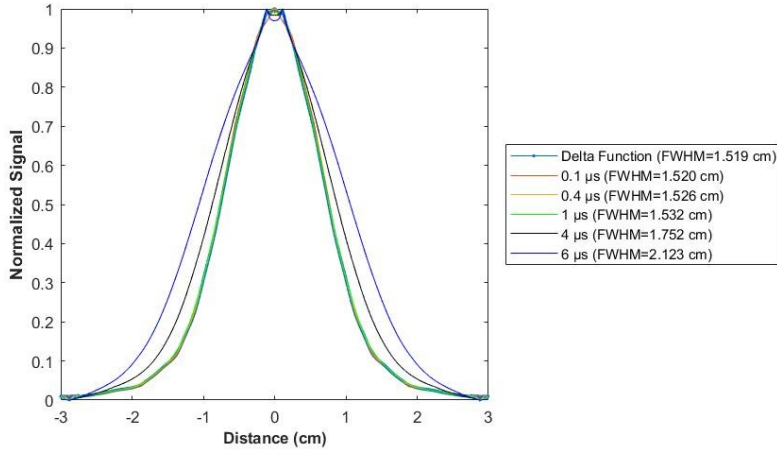
Figure 14: a) The reconstructed pressure-based percent depth curve for the different linac pulse durations relative to the Monte Carlo-based PDD curve. b) The reconstructed pressure-based percent depth curve normalized to the 1 cm depth signal for the different linac pulse durations corrected for the pulse duration shift with temporal linac pulse deconvolution and compared relative to the Monte Carlo-based PDD curve.   21
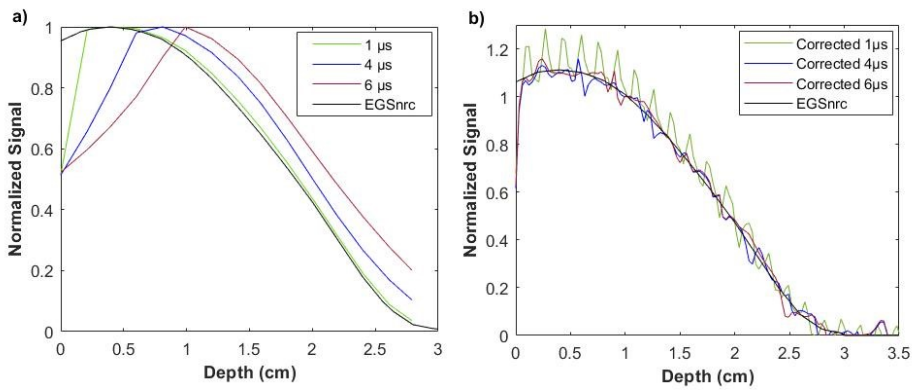
Table 3: The material characteristics of the gelatin phantom

Density (ρ)	1035 g/cm^3
Sound speed (Cs)	1562 m/s
Grüneisen coefficient (Γ)	0.22
Attenuation coefficient (α)	0.58 dB/MHz^y -cm
Attenuation power (y)*	1.3

* y is a frequency dependent exponent of the acoustic attenuation power law. It is a real non-negative

material dependent parameter that ranges from 0 to 2.

Table 4: Percent of points in the reconstructed image passing Gamma test criteria between the reconstructed spatial pressure distribution and the relative dose distribution levels for the five different linac pulse durations.

Pulse duration(μs)	% of Points Passing the Gamma Criteria		
	3%/3mm	1%/1mm	0.5%/0.5mm
0.1	100	97.3	93.9
0.4	100	97.5	91.6
1	100	97.8	87.0
4	100	55.9	30.1
6	67.4	43.7	23.7